Itinerant ferromagnetism and $p + ip'$ superconductivity in doped bilayer silicene

Li-Da Zhang, Fan Yang,* and Yugui Yao†
School of Physics, Beijing Institute of Technology, Beijing 100081, China
(Received 23 May 2015; revised manuscript received 25 June 2015; published 4 September 2015)

We study the electronic instabilities of doped bilayer silicene using the random phase approximation. In contrast to the singlet $d + id'$ superconductivity at the low doping region, we find that the system is an itinerant ferromagnet in the narrow doping regions around the Van Hove singularities, and a triplet $p + ip'$ superconductor in the vicinity of these regions. Adding a weak Kane-Mele spin-orbit coupling to the system further singles out the time-reversal invariant equal-spin helical $p + ip'$ pairing as the leading instability. The triplet pairing identified here is driven by the ferromagnetic fluctuations, which become strong and enhance the superconducting critical temperature remarkably near the phase boundaries between ferromagnetism and superconductivity.

DOI: 10.1103/PhysRevB.92.104504 PACS number(s): 74.20.Rp, 74.25.Dw, 75.10.Lp

I. INTRODUCTION

Magnetism and unconventional superconductivity (SC) as well as the intimate interplay between them have been the focuses of condensed matter physics for decades due to their rich physics and important applications. Among these subjects, the realizations of itinerant ferromagnetism (FM) and triplet SC are of particular importance in recent years. In general, the triplet SC [1], which is connected with topological SC [2,3] and has become a hot topic recently, is believed to be driven by ferromagnetic spin fluctuations near the ferromagnetic order. However, the realization of itinerant FM from the Stoner criterion [4] usually requires finite and, most of the time, strong electron interaction [5–13], which is hard to deal with in the weak coupling perturbative approaches. One way to overcome this difficulty is to introduce the divergent density of states (DOS) at the Van Hove (VH) singularities of the system, which can induce these instabilities without strong electronic interaction. It's proposed recently that, for a system with its Fermi surface (FS) doped to time-reversal (TR) variant VH saddle points, weak repulsive electron interactions can usually drive itinerant FM and triplet SC [14].

On another front, as the Si-based counterpart of graphene, silicene has been synthesized recently [15–19], with experimental evidence showing possible SC in the doped case [20], which has attracted a lot of research interest [21–25]. Furthermore, bilayer silicene (BLS) has also been available [26], with the energetically most favored stacking way between its two layers identified by first-principles calculations [27]. Based on the metallic band structure of undoped BLS, the antiferromagnetism and the chiral $d + id'$ SC tuned by strain have been proposed [27]. This intriguing result motivates us to further investigate the electronic instabilities in doped BLS, specifically focusing on the VH doping levels since the divergent DOS there favors the occurrence of electronic instabilities. Turning our attention to VH doping, we notice that, in VH-doped monolayer graphene whose VH saddle points locate at TR invariant momenta, the chiral spin density wave or the chiral $d + id'$ pairing has been proposed [28–32]. Similar results have also been found in monolayer silicene [33]. In contrast, the interesting property of the VH singularities here in BLS lies in that the VH saddle points locate at TR variant momenta. For such VH singularities, the study based on the renormalization group theory has pointed out the possibility of the formation of itinerant FM and triplet SC [14].

In this paper, we perform the calculations based on the random phase approximation (RPA) to investigate possible electronic instabilities of doped BLS. The main results of our calculations are as follows. In addition to the $d + id'$ SC occurring at low doping levels, the itinerant FM and the triplet $p + ip'$ SC emerge as the leading instabilities of the system in the narrow doping regions around the VH singularities and the vicinity of these regions, respectively. In the presence of a weak Kane-Mele spin-orbit coupling (SOC) [34,35], the equal-spin helical $p + ip'$ pairing wins over the chiral one and serves as the leading instability of the system. The emergence of the FM and the triplet SC results from the large DOS and the strong ferromagnetic correlation around the VH singularities. Near the critical doping level separating the FM and triplet SC, the strong ferromagnetic fluctuations will greatly enhance the superconducting critical temperature, which provides possibility to realize this triplet $p + ip'$ pairing state at experimentally accessible temperatures.

The rest of this paper is organized as follows. In Sec. II, we describe the Hubbard model of BLS, as well as the RPA approach. In Sec. III, we calculate the susceptibilities of the system and demonstrate the itinerant FM occurring around the VH singularities. In Sec. IV, we study the superconducting pairing symmetries for different doping levels and propose that the $p + ip'$ pairing dominates over the $d + id'$ one in the vicinity of the ferromagnetic regions. Finally, in Sec. V, a conclusion will be reached after discussions on the experimental detection of the novel $p + ip'$ pairing state proposed here.

II. MODEL AND APPROACH

The lattice structure of BLS is shown in Fig. 1(a), which belongs to the D_{3d} point group [27]. While sublattice A_1 of the upper silicene layer couples vertically to sublattice A_2 of the lower layer with a bond-length $l_v = 2.52$ Å, the two sublattices A_l and B_l within the same layer l (= 1,2) couple to each other with a bond-length $l_n = 2.32$ Å. Approximately

*yangfan_blg@bit.edu.cn
†ygyao@bit.edu.cn

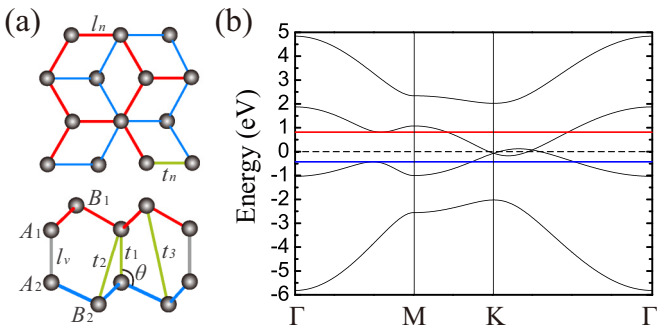

FIG. 1. (Color online) (a) The lattice structure of BLS. (b) The corresponding band structure. In (a), both the top view (upper) and side view (lower) are shown. The intralayer nearest-neighbor bond length l_n, the vertical bond length l_v, and the angle θ between them are marked, together with the hopping integrals t_n, t_1, t_2, and t_3. In (b), the black dashed, red and blue solid horizontal lines denote the Fermi levels of the undoped, electron and hole VH-doped systems, respectively.

equal bond lengths, together with the bond-angle $\theta = 106.65^\circ$ between the two bonds describe an orbital hybridization more like the sp^3 type than the planar sp^2 one. This lattice structure leads to a strong interlayer coupling, and the resulting strong bonding-antibonding splitting between orbitals A_1 and A_2 pushes them far away from the Fermi level. Thus, the low-energy subspace formed by orbitals B_1 and B_2 will take responsibility for the main physics of the system [27]. This feature of BLS is obviously different from that of bilayer graphene.

According to Ref. [27], the low-energy physics of BLS near the FS can be described by the following four-band Hubbard model of the system:

$$H = \sum_{\boldsymbol{k}\sigma\alpha\beta} c^{\dagger}_{\boldsymbol{k}\alpha\sigma} H_{\alpha\beta}(\boldsymbol{k}) c_{\boldsymbol{k}\beta\sigma} + U \sum_{i\alpha} n_{i\alpha\uparrow} n_{i\alpha\downarrow}. \quad (1)$$

Here σ, α (β), and i denote the spin, orbital, and unit cell indices, respectively, and $H(\boldsymbol{k})$ is the four-band tight-binding (TB) Hamiltonian in the basis $\{|B_1\rangle, |B_2\rangle, |A_1\rangle, |A_2\rangle\}$. The explicit expression of the TB Hamiltonian reads [27]

$$H(\boldsymbol{k}) = \begin{pmatrix} \Delta & t_3 f(\boldsymbol{k}) & t_n f(\boldsymbol{k})^* & -t_2 f(\boldsymbol{k})^* \\ t_3 f(\boldsymbol{k})^* & \Delta & -t_2 f(\boldsymbol{k}) & t_n f(\boldsymbol{k}) \\ t_n f(\boldsymbol{k}) & -t_2 f(\boldsymbol{k})^* & 0 & t_1 \\ -t_2 f(\boldsymbol{k}) & t_n f(\boldsymbol{k})^* & t_1 & 0 \end{pmatrix}. \quad (2)$$

Here $f(\boldsymbol{k}) = \sum_\alpha e^{i\boldsymbol{k}\cdot\boldsymbol{R}_\alpha}$ with $\boldsymbol{R}_\alpha$ ($\alpha = 1,2,3$) being the nearest-neighbor vector, $\Delta = -0.069$ eV is the effective on-site energy difference between atoms A_l and B_l, the hopping integrals $t_n = 1.130$ eV, $t_1 = 2.025$ eV, $t_2 = 0.152$ eV, and $t_3 = 0.616$ eV. Since the basis $\{|B_1\rangle, |B_2\rangle, |A_1\rangle, |A_2\rangle\}$ is mainly composed of the $3p_z$ orbital of silicon [36], we set $U = 1$ eV as a rough estimate of the Hubbard interaction.

The band structure for the above TB Hamiltonian Eq. (2) is shown in Fig. 1(b). One feature of the band structure is the 300 meV overlap between the valence and conduction bands near the K points. For the undoped case, this overlap causes six pairs of small electron and hole pockets around

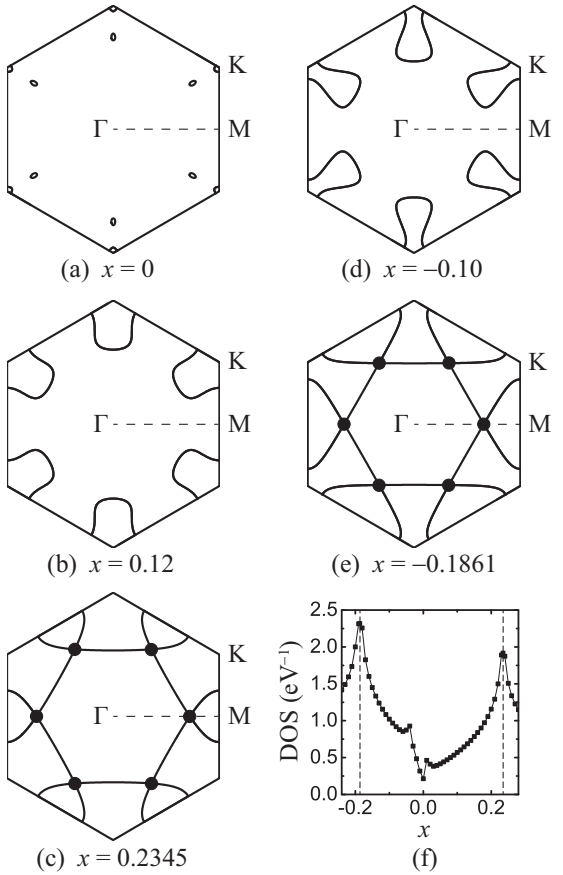

FIG. 2. (a)–(e) The shapes of the FS for different doping levels. The black dots in (c) and (e) indicate the VH saddle points. (f) The doping dependence of the DOS near the FS. The vertical dashed lines indicate the VH singularities.

and near the K points, respectively, as shown in Fig. 2(a). The undoped system is thus intrinsically metallic and can enter a superconducting state [27]. When the system is doped, regardless of electron or hole doping case, the shape of the FS grows gradually from separated electron and hole pockets first to six big merged pockets around the K points [Figs. 2(b) and 2(d)], which finally connect to one another at the VH saddle points, causing the Lifshits transition of the FS [Figs. 2(c) and 2(e)]. Defining the doping level by $x = n_e - 1$, where n_e is the number of electrons per site, we find the doping levels for the VH singularities are $x = 0.2345$ for electron doping and $x = -0.1861$ for hole doping, respectively. The Fermi levels for these VH dopings are marked in Fig. 1(b), where the flatness of the bands near the VH singularities leads to the logarithmically divergent DOS there as shown in Fig. 2(f). We shall focus on these VH dopings in the following study because the divergent DOS around there urges the formation of itinerant FM, and the resulting strong ferromagnetic fluctuations in the vicinity of the FM regions will induce high-temperature triplet SC.

A special feature of the VH singularities of BLS lies in that its VH saddle points locate on the M-Γ axes rather than at the TR invariant M points as in bilayer graphene as well as monolayer graphene or silicene. Such TR variant VH saddle points are named as "type-II" VH saddle points in Ref. [14],

in contrast to the TR invariant "type-I" VH saddle points. The "type-II" VH singularity is special in that it allows for the formation of triplet SC. If the FS of a system contains TR invariant "type-I" VH saddle points, the triplet pairing will not be energetically favored because its odd parity gap function will have nodes at these TR invariant VH momenta, which is no good for the energy gain. On the contrary, the TR variant "type-II" VH saddle points of BLS locating on the M-Γ axes provide the possibility for the system to enter the triplet pairing state.

To study the electron instabilities of the system described by the Hubbard model Eq. (1), we adopt the standard multiorbital RPA approach [27,37–41]. We first define and calculate the bare susceptibility tensor $\chi^{(0)l_1,l_2}_{l_3,l_4}(\boldsymbol{q},\tau)$. After that, the renormalized charge (c) or spin (s) susceptibility $\chi^{(c(s))l_1,l_2}_{l_3,l_4}(\boldsymbol{q},\tau)$ is obtained in the RPA level. For each doping level, there will be a critical interaction strength U_c. For repulsive $U > U_c$, the renormalized spin susceptibility diverges, implying the formation of long-range magnetic order. For $U < U_c$, through exchanging the charge or spin fluctuations, we obtain the effective pairing potential $V^{\alpha\beta}(\boldsymbol{k},\boldsymbol{q})$. Solving the linearized gap equation for $V^{\alpha\beta}(\boldsymbol{k},\boldsymbol{q})$ as an eigenvalue problem, we obtain the leading pairing gap function as the eigenvector corresponding to the largest eigenvalue.

III. ITINERANT FERROMAGNETISM

The bare ($U = 0$) susceptibility tensor of model Eq. (1) is defined as

$$\chi^{(0)pq}_{st}(\boldsymbol{k},\tau) \equiv \frac{1}{N}\sum_{\boldsymbol{k}_1\boldsymbol{k}_2}\langle T_\tau c^\dagger_p(\boldsymbol{k}_1,\tau)c_q(\boldsymbol{k}_1+\boldsymbol{k},\tau) \times c^\dagger_s(\boldsymbol{k}_2+\boldsymbol{k},0)c_t(\boldsymbol{k}_2,0)\rangle_0, \quad (3)$$

Here $\langle\cdots\rangle_0$ denotes the thermal average for $U = 0$, T_τ denotes the time-ordered product, and $p,q,s,t = 1,\cdots,4$ are the sublattice indices. Fourier transformed to the imaginary frequency space, the bare susceptibility can be expressed by the following explicit formulism,

$$\chi^{(0)pq}_{st}(\boldsymbol{k},i\omega_n) = \frac{1}{N}\sum_{\boldsymbol{k}'\alpha\beta}\xi^\alpha_t(\boldsymbol{k}')\xi^{\alpha*}_p(\boldsymbol{k}')\xi^\beta_q(\boldsymbol{k}'+\boldsymbol{k}) \times \xi^{\beta*}_s(\boldsymbol{k}'+\boldsymbol{k})\frac{n_F\left(\varepsilon^\beta_{\boldsymbol{k}'+\boldsymbol{k}}\right)-n_F\left(\varepsilon^\alpha_{\boldsymbol{k}'}\right)}{i\omega_n+\varepsilon^\alpha_{\boldsymbol{k}'}-\varepsilon^\beta_{\boldsymbol{k}'+\boldsymbol{k}}}. \quad (4)$$

Here $i\omega_n$ is the Matsubara frequency, $\alpha,\beta = 1,\cdots,4$ are the band indices, n_F is the Fermi distribution function, and $\varepsilon^\alpha_{\boldsymbol{k}}$ and $\xi^\alpha(\boldsymbol{k})$ are the eigenvalue and eigenvector of the TB Hamiltonian Eq. (2). The Hermitian static susceptibility matrix is defined as $\chi^{(0)}_{p,s}(\boldsymbol{k}) \equiv \chi^{(0)pp}_{ss}(\boldsymbol{k},i\omega_n = 0)$. For each $\boldsymbol{k}$, the largest eigenvalue $\chi^{(0)}(\boldsymbol{k})$ of this matrix represents the static susceptibility of the system in the strongest channel, and the corresponding eigenvector describes the pattern of the dominant intrinsic spin correlation in a unit cell of the system.

In Figs. 3(a)–3(e), we show the $\boldsymbol{k}$-space distributions of the zero-temperature static susceptibility $\chi^{(0)}(\boldsymbol{k})$ for different doping levels, which reveal the doping evolution of the static susceptibility. In particular, when the doping level changes gradually from zero to the VH doping, regardless of electron or hole doping case, the momenta of the maximum susceptibility evolve from the Γ point [Fig. 3(a)] first to the points around it [Figs. 3(b) and 3(d)], and finally back to the Γ point again [Figs. 3(c) and 3(e)]. Such a doping evolution of the susceptibility originates from the evolution of the FS mentioned before and indicates that the intrasublattice spin correlation of the system changes gradually with doping from ferromagnetic first to antiferromagnetic, and finally back to ferromagnetic again.

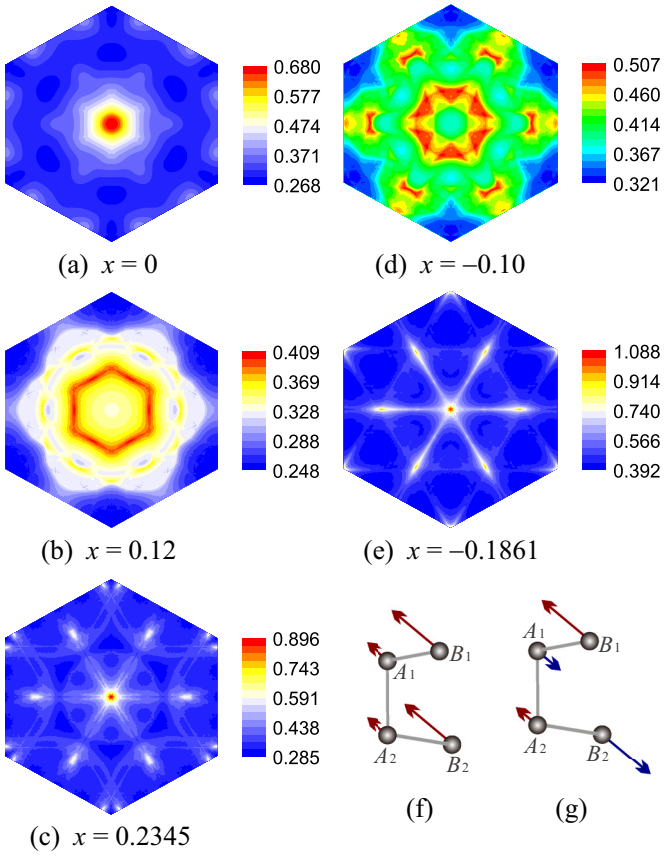

FIG. 3. (Color online) (a)–(e) The $\boldsymbol{k}$-space distributions of the zero-temperature static susceptibility $\chi^{(0)}(\boldsymbol{k})$ for different doping levels. Typical (f) ferromagnetic pattern at the VH doping levels and (g) antiferromagnetic pattern at zero doping in a unit cell of the system.

From the eigenvector corresponding to the largest eigenvalue of $\chi^{(0)}_{p,s}(\boldsymbol{k})$, we find that the spin correlation within a unit cell is ferromagnetic-like [see Fig. 3(f)] near the VH doping levels, and antiferromagnetic-like [see Fig. 3(g)] near zero doping. Therefore, although the intrasublattice spin correlations in both the VH-doped and undoped systems are ferromagnetic, the intersublattice spin correlations in the former and latter cases are ferromagnetic and antiferromagnetic, respectively.

When the interaction is turned on, we define the charge (c) and spin (s) susceptibilities of model Eq. (1) as

$$\chi^{(c)pq}_{st}(\boldsymbol{k},\tau) \equiv \frac{1}{2N}\sum_{\boldsymbol{k}_1\boldsymbol{k}_2\sigma_1\sigma_2}\langle T_\tau c^\dagger_{p\sigma_1}(\boldsymbol{k}_1,\tau) \times c_{q\sigma_1}(\boldsymbol{k}_1+\boldsymbol{k},\tau)c^\dagger_{s\sigma_2}(\boldsymbol{k}_2+\boldsymbol{k},0)c_{t\sigma_2}(\boldsymbol{k}_2,0)\rangle, \quad (5)$$

$$\chi_{st}^{(s^z)pq}(\boldsymbol{k},\tau) \equiv \frac{1}{2N}\sum_{\boldsymbol{k}_1\boldsymbol{k}_2\sigma_1\sigma_2}\sigma_1\sigma_2\langle T_\tau c^\dagger_{p\sigma_1}(\boldsymbol{k}_1,\tau) \times c_{q\sigma_1}(\boldsymbol{k}_1+\boldsymbol{k},\tau)c^\dagger_{s\sigma_2}(\boldsymbol{k}_2+\boldsymbol{k},0)c_{t\sigma_2}(\boldsymbol{k}_2,0)\rangle, \quad (6)$$

$$\chi_{st}^{(s^{+-})pq}(\boldsymbol{k},\tau) \equiv \frac{1}{N}\sum_{\boldsymbol{k}_1\boldsymbol{k}_2}\langle T_\tau c^\dagger_{p\uparrow}(\boldsymbol{k}_1,\tau) \times c_{q\downarrow}(\boldsymbol{k}_1+\boldsymbol{k},\tau)c^\dagger_{s\downarrow}(\boldsymbol{k}_2+\boldsymbol{k},0)c_{t\uparrow}(\boldsymbol{k}_2,0)\rangle, \quad (7)$$

$$\chi_{st}^{(s^{-+})pq}(\boldsymbol{k},\tau) \equiv \frac{1}{N}\sum_{\boldsymbol{k}_1\boldsymbol{k}_2}\langle T_\tau c^\dagger_{p\downarrow}(\boldsymbol{k}_1,\tau) \times c_{q\uparrow}(\boldsymbol{k}_1+\boldsymbol{k},\tau)c^\dagger_{s\uparrow}(\boldsymbol{k}_2+\boldsymbol{k},0)c_{t\downarrow}(\boldsymbol{k}_2,0)\rangle, \quad (8)$$

where $\sigma_1, \sigma_2 = \uparrow, \downarrow$ are spin indices. For nonmagnetic states, we have $\chi^{(s^z)} = \chi^{(s^{+-})} = \chi^{(s^{-+})} \equiv \chi^{(s)}$. For $U = 0$, we further have $\chi^{(c)} = \chi^{(s)} = \chi^{(0)}$.

In the standard RPA approach [27,37–41], the charge (spin) susceptibility of model Eq. (1) is given by

$$\chi^{(c(s))}(\boldsymbol{k},i\omega_n) = [I \pm \chi^{(0)}(\boldsymbol{k},i\omega_n)(U)]^{-1}\chi^{(0)}(\boldsymbol{k},i\omega_n), \quad (9)$$

where (U) is a 16×16 matrix, whose only four nonzero elements are $(U)^{\mu\mu}_{\mu\mu} = U$ $(\mu = 1,\cdots,4)$ [27]. Clearly, the repulsive Hubbard interaction here suppresses $\chi^{(c)}$ and enhances $\chi^{(s)}$. When the interaction parameter U is weak enough, the RPA works well since all eigenvalues of the denominator matrix $[I \pm \chi^{(0)}(\boldsymbol{k},i\omega_n)(U)]$ in Eq. (9) are positive and hence the matrix itself has an inverse. However, if U exceeds a critical value U_c at which the lowest eigenvalue of $[I - \chi^{(0)}(\boldsymbol{k},i\omega_n)(U)]$ touches zero, the renormalized spin susceptibility $\chi^{(s)}$ will diverge, which implies the formation of long-range magnetic order.

The doping dependence of the critical interaction strength U_c is shown in Fig. 4. The most obvious feature of Fig. 4 is that U_c drops abruptly to zero near the VH singularities due to the divergent DOS there. For $U = 1$ eV adopted in our calculation, the U_c drops below U in narrow doping regions around the VH singularities, which will lead to long-range magnetic order. Furthermore, from the ferromagnetic correlation near the VH singularities revealed by $\chi^{(0)}$ shown in Figs. 3(c), 3(e), and 3(f), we conclude that long-range itinerant FM will emerge in these narrow doping regions.

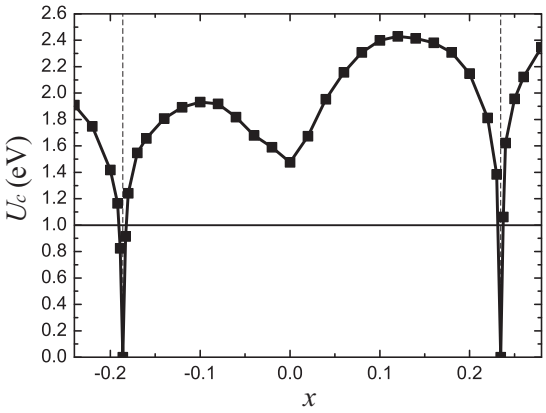

FIG. 4. The doping dependence of the magnetic critical interaction strength U_c. The horizontal solid line indicates $U = 1$ eV, and the vertical dashed lines indicate the VH singularities.

IV. TRIPLET $p + ip'$ SC

Away from the above introduced narrow doping regions for itinerant FM, the interaction strength $U = 1$ eV is smaller than the critical value U_c as shown in Fig. 4. Then through exchanging short-range spin or charge fluctuations between a Cooper pair, exotic superconducting states will emerge in the system. More specifically, we consider the scattering of a Cooper pair from the state $(\boldsymbol{k}', -\boldsymbol{k}')$ in the βth $(\beta = 1,\cdots,4)$ band to the state $(\boldsymbol{k}, -\boldsymbol{k})$ in the αth $(\alpha = 1,\cdots,4)$ band via exchanging spin or charge fluctuations. This scattering process leads to the following effective interaction vertex [41]:

$$V^{\alpha\beta}(\boldsymbol{k},\boldsymbol{k}') = \mathrm{Re}\sum_{pqst}\Gamma^{pq}_{st}(\boldsymbol{k},\boldsymbol{k}')\xi^{\alpha*}_p(\boldsymbol{k}) \times \xi^{\alpha*}_q(-\boldsymbol{k})\xi^{\beta}_s(-\boldsymbol{k}')\xi^{\beta}_t(\boldsymbol{k}'). \quad (10)$$

Here, for the singlet channel, we have

$$\Gamma^{pq}_{st}(\boldsymbol{k},\boldsymbol{k}') = (U)^{pt}_{qs} + \tfrac{1}{4}[3(U)(\chi^{(s)} - \chi^{(c)})(U)]^{pt}_{qs}(\boldsymbol{k}-\boldsymbol{k}') + \tfrac{1}{4}[3(U)(\chi^{(s)} - \chi^{(c)})(U)]^{ps}_{qt}(\boldsymbol{k}+\boldsymbol{k}'), \quad (11)$$

and for the triplet channel, we have

$$\Gamma^{pq}_{st}(\boldsymbol{k},\boldsymbol{k}') = -\tfrac{1}{4}[(U)(\chi^{(s)} + \chi^{(c)})(U)]^{pt}_{qs}(\boldsymbol{k}-\boldsymbol{k}') + \tfrac{1}{4}[(U)(\chi^{(s)} + \chi^{(c)})(U)]^{ps}_{qt}(\boldsymbol{k}+\boldsymbol{k}'). \quad (12)$$

From the effective interaction vertex Eq. (10), we obtain the following linearized gap equation [40] near the superconducting critical temperature T_c:

$$-\frac{1}{(2\pi)^2}\sum_\beta\oint_{FS}dk'_\parallel\frac{V^{\alpha\beta}(\boldsymbol{k},\boldsymbol{k}')}{v^\beta_F(\boldsymbol{k}')}\Delta_\beta(\boldsymbol{k}') = \lambda\Delta_\alpha(\boldsymbol{k}). \quad (13)$$

Here the integration is along various FS patches labeled by α or β, $v^\beta_F(\boldsymbol{k}')$ is the Fermi velocity, and $k'_\parallel$ is the component of $\boldsymbol{k}'$ along the FS. Solving this gap equation as an eigenvalue problem, one obtains each pairing eigenvalue λ and the corresponding normalized eigenvector $\Delta_\alpha(\boldsymbol{k})$ as the relative pairing gap function. The leading pairing symmetry is determined by the $\Delta_\alpha(\boldsymbol{k})$ corresponding to the largest λ. The critical temperature T_c is determined by λ through $T_c =$ cutoff energy $\cdot e^{-1/\lambda}$, where the cutoff energy scales with the low-energy bandwidth.

Consistent with the D_{3d} point group of the system, the pairing symmetries obtained from Eq. (13) are s, p, d, and f waves. More specifically, in the vicinity of the narrow doping regions for itinerant FM around the VH singularities, we identify the doubly degenerate p_x and p_y triplet pairings as the leading pairing symmetries. The gap function of the p_x (p_y) symmetry is symmetric about the x (y) axis and antisymmetric about the y (x) axis, with gap nodes on the y (x) axis, as shown in Fig. 5(a) [5(b)]. On the other hand, at the low doping region, we identify the doubly degenerate $d_{x^2-y^2}$ and d_{xy} singlet pairings as the leading pairing symmetries. The gap functions of the $d_{x^2-y^2}$ and d_{xy} symmetries are symmetric

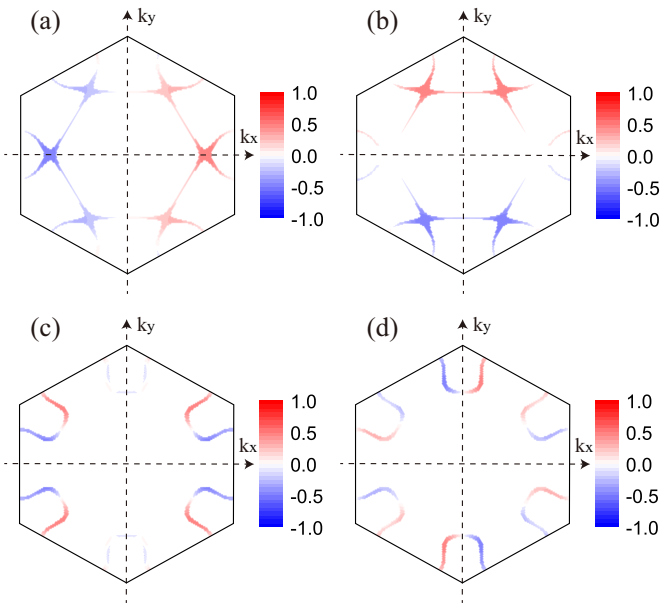

FIG. 5. (Color online) Distributions of the gap functions on the FS: (a) p_x and (b) p_y symmetries for doping $x = 0.24$, as well as (c) $d_{x^2-y^2}$ and (d) d_{xy} symmetries for doping $x = 0.12$.

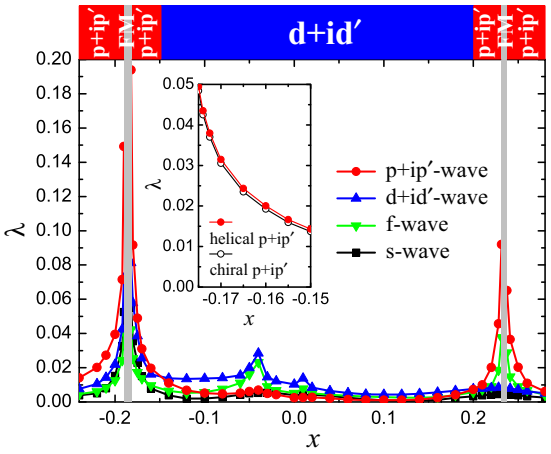

FIG. 6. (Color online) The doping dependence of the pairing eigenvalues λ of all possible pairing symmetries in the system. The vertical bold gray lines indicate the doping regions where the itinerant FM occurs. Inset: the typical split between the helical $(p_x+ip_y)_{\uparrow\uparrow}$,$(p_x-ip_y)_{\downarrow\downarrow}$ pairing and the chiral $(p_x\pm ip_y)_{(\uparrow\downarrow+\downarrow\uparrow)}$ pairing caused by the weak SOC term with $\lambda_{\rm SO} = 10$ meV. The split in other doping regions where the $p+ip'$ SC occurs is similar to the one shown in the inset.

and antisymmetric about both the x and y axes respectively, as shown in Figs. 5(c) and 5(d).

Since the p_x and p_y pairing states are degenerate, they will probably mix to lower the energy below the critical temperature T_c. To determine this mixture, we set $\Delta_{\boldsymbol{k}}^{\alpha} = K_1 p_x^{\alpha}(\boldsymbol{k}) + (K_2 + iK_3) p_y^{\alpha}(\boldsymbol{k})$, where $p_x^{\alpha}(\boldsymbol{k})$ and $p_y^{\alpha}(\boldsymbol{k})$ denote the normalized gap functions of corresponding symmetries. Then the mixing coefficients K_1, K_2, and K_3 are determined by the minimization of the total mean-field energy,

$$E = \sum_{\boldsymbol{k}\alpha} \varepsilon_{\boldsymbol{k}}^{\alpha} \left[1 - \frac{\varepsilon_{\boldsymbol{k}}^{\alpha} - \mu}{\sqrt{\left(\varepsilon_{\boldsymbol{k}}^{\alpha} - \mu\right)^2 + \left|\Delta_{\boldsymbol{k}}^{\alpha}\right|^2}} \right] + \frac{1}{4N} \sum_{\boldsymbol{k}\boldsymbol{k}'\alpha\beta} V^{\alpha\beta}(\boldsymbol{k},\boldsymbol{k}') \times \frac{\left(\Delta_{\boldsymbol{k}}^{\alpha}\right)^*}{\sqrt{\left(\varepsilon_{\boldsymbol{k}}^{\alpha} - \mu\right)^2 + \left|\Delta_{\boldsymbol{k}}^{\alpha}\right|^2}} \frac{\Delta_{\boldsymbol{k}'}^{\beta}}{\sqrt{\left(\varepsilon_{\boldsymbol{k}'}^{\beta} - \mu\right)^2 + \left|\Delta_{\boldsymbol{k}'}^{\beta}\right|^2}}. \quad (14)$$

Here the chemical potential μ is determined by the constraint of the average electron number in the superconducting state. Our energy minimization gives $K_1 = \pm K_3$ and $K_2 = 0$, which leads to the fully gapped $p_x \pm ip_y$ (abbreviated as $p+ip'$) SC. This mixture of the two p-wave pairings satisfies the requirement that the gap nodes should avoid the FS to lower the energy. Physically, the triplet $p+ip'$ pairing is mediated by the strong ferromagnetic spin fluctuations near the VH singularities, as revealed by Figs. 3(c), 3(e), and 3(f). Similar to the above p-wave pairings, below T_c, the degenerate $d_{x^2-y^2}$ and d_{xy} pairing states will also mix into the fully gapped $d_{x^2-y^2} \pm id_{xy}$ (abbreviated as $d+id'$) pairing to lower the energy, which is consistent with our previous results for the undoped case [27]. Physically, the singlet $d+id'$ pairing is mediated by the antiferromagnetic spin fluctuations suggested by Figs. 3(a), 3(b), 3(d), and 3(g).

In Fig. 6, we show the doping dependence of the pairing eigenvalues of all possible pairing symmetries in the system, including $p+ip'$, $d+id'$, f, and s waves. It is interesting to note that the pairing eigenvalue of the $p+ip'$ pairing diverges in the doping regions near the phase boundaries between FM and SC, due to the divergently strong ferromagnetic spin fluctuations in these regions. Although this divergence is an artifact in the RPA caused by ignorance of the renormalization of the single-particle Green's function, it is possible that the strong ferromagnetic fluctuations in the critical regions push the superconducting critical temperature T_c up to values accessible in experiments. Taking into account that the doping level is hard to control in practice, we can instead apply tunable strain to the system to change the hopping parameters and the band structure [27]. As a result, the VH doping levels and the phase boundaries between FM and SC will shift so that a given doping level can access the phase boundaries to produce the high-temperature triplet $p+ip'$ SC.

Note that there are three different components of the triplet $p+ip'$ pairing, each with a different spin S_z quantum number of the Cooper pair labeled by $\uparrow\uparrow$, $\downarrow\downarrow$, or $(\uparrow\downarrow + \downarrow\uparrow)$. In the absence of SOC, the three spin components are degenerate. To lift up this degeneracy, we need to add an extra SOC term to Hamiltonian Eq. (1). The inversion symmetry of the system rules out the Rashba SOC, and thus leaves the proper form of the SOC term as the following Kane-Mele one [34,35]:

$$H_{\rm KM} = i\lambda_{\rm SO} \sum_{\langle\langle ij \rangle\rangle} \nu_{ij} c_i^{\dagger} \sigma^z c_j. \quad (15)$$

Here $\nu_{ij} = (2/\sqrt{3})(\hat{\boldsymbol{b}}_1 \times \hat{\boldsymbol{b}}_2)_z = \pm 1$ with $\hat{\boldsymbol{b}}_1$ and $\hat{\boldsymbol{b}}_2$ being unit vectors along the two bonds that connect next-nearest neighbors i and j on the same layer. Such a SOC term lifts up

the degeneracy between the $S_z = 0$ component and $S_z = \pm 1$ components. Our RPA calculations (see the Appendix for the details) reveal that the equal-spin helical $(p_x + ip_y)_{\uparrow\uparrow}$, $(p_x - ip_y)_{\downarrow\downarrow}$ pairing wins over the chiral $(p_x \pm ip_y)_{(\uparrow\downarrow+\downarrow\uparrow)}$ pairing by a small split proportional to $\lambda_{SO} = 10$ meV as shown in the insets of Fig. 6. Such a helical triplet pairing leads to TR invariant weak topological SC of the system.

V. DISCUSSION AND CONCLUSION

The unconventional triplet $p + ip'$ SC proposed here can be detected by various experiments. First of all, as an unconventional superconducting state with the phase of its pairing gap function changing on the FS, the $p + ip'$ pairing state should show no Hebel-Slichter peak in the NMR relaxation rate $1/T_1T$ upon the superconducting phase transition [42]. Second, in this triplet pairing state, the Knight shift should not obviously change below the T_c [43]. To further identify the phase structure of this pairing experimentally, we can fabricate a slice of BLS into a hexagon, and use a dc SQUID to detect the relative phase among different directions in the system [44]. In particular, determined by the $p + ip'$ symmetry, the phase difference between the opposite (adjacent) edges of the hexagon should be π ($\pi/3$).

Although the p-wave SC is unconventional, the mixing of the p_x and p_y pairings into the complex $p + ip'$ one leads to a fully gapped superconducting state, which looks similar to the conventional s-wave one in many aspects. For example, near zero temperature, the specific heat, the penetration depth, and the NMR relaxation rate of both fully gapped pairing states decay exponentially with temperature. What's more, the STM spectra of both fully gapped superconducting states should exhibit U-shaped $dI/dV - V$ curves. However, all these expected experimental results can be changed by a uniaxial strain applied on the system. More specifically, the $p + ip'$ mixing proposed here is based on the degeneracy between the p_x and p_y pairing states, and the degeneracy itself originates from the D_{3d} point group of the system [27]. Thus, by applying a uniaxial strain to break the D_{3d} symmetry, we can eliminate the $p + ip'$ mixing, and leave a single real p-wave pairing as the leading instability. Such a p-wave pairing can be the p_x or p_y one, which is determined by the axis of the applied strain. Because the resulting p_x or p_y pairing has gap nodes on the FS, the above-mentioned exponential temperature dependence of the experimental observables of the system will be replaced by a power-law one. Meanwhile, the U-shaped STM spectrum of the system will be replaced by a V-shaped one.

In conclusion, we have systematically studied the possible electronic instabilities of doped BLS. The results of our RPA calculations predict that the system is an itinerant ferromagnet in the narrow doping regions around the VH singularities, and a triplet $p + ip'$ superconductor with a possible high T_c in the vicinity of these regions. With an extra weak Kane-Mele SOC, we further single out the equal-spin helical $p + ip'$ pairing state as the leading one. This intriguing triplet superconducting state has TR-invariant weak topological property and can harbor the Majorana zero-mode at its boundary [3,45–47], which is useful in the topological quantum computation.

ACKNOWLEDGMENTS

This work is supported by the MOST Project of China (Grants No. 2014CB920903 and No. 2011CBA00100), the National Natural Science Foundation of China (Grants No. 11274041, No. 11174337, No. 11225418, and No. 11334012), and the Specialized Research Fund for the Doctoral Program of Higher Education of China (Grants No. 20121101110046 and No. 20121101120046). F.Y. is also supported by the NCET program under Grant No. NCET-12-0038.

APPENDIX: RPA WITH THE KANE-MELE SOC

The Kane-Mele SOC term breaks the $SU(2)$ spin-rotation symmetry but keeps the $U(1)$ spin-rotation symmetry around the S_z axis [34,35]. Since the S_z component of the total spin is a good quantum number, we define the following susceptibility tensors:

$$\chi_{st}^{(1)pq}(\boldsymbol{k},\tau) \equiv \frac{1}{N}\sum_{\boldsymbol{k}_1\boldsymbol{k}_2}\langle T_\tau c_{p\uparrow}^\dagger(\boldsymbol{k}_1,\tau)c_{q\uparrow}(\boldsymbol{k}_1+\boldsymbol{k},\tau) \times c_{s\uparrow}^\dagger(\boldsymbol{k}_2+\boldsymbol{k},0)c_{t\uparrow}(\boldsymbol{k}_2,0)\rangle, \tag{A1}$$

$$\chi_{st}^{(2)pq}(\boldsymbol{k},\tau) \equiv \frac{1}{N}\sum_{\boldsymbol{k}_1\boldsymbol{k}_2}\langle T_\tau c_{p\uparrow}^\dagger(\boldsymbol{k}_1,\tau)c_{q\uparrow}(\boldsymbol{k}_1+\boldsymbol{k},\tau) \times c_{s\downarrow}^\dagger(\boldsymbol{k}_2+\boldsymbol{k},0)c_{t\downarrow}(\boldsymbol{k}_2,0)\rangle, \tag{A2}$$

$$\chi_{st}^{(3)pq}(\boldsymbol{k},\tau) \equiv \frac{1}{N}\sum_{\boldsymbol{k}_1\boldsymbol{k}_2}\langle T_\tau c_{p\downarrow}^\dagger(\boldsymbol{k}_1,\tau)c_{q\downarrow}(\boldsymbol{k}_1+\boldsymbol{k},\tau) \times c_{s\uparrow}^\dagger(\boldsymbol{k}_2+\boldsymbol{k},0)c_{t\uparrow}(\boldsymbol{k}_2,0)\rangle, \tag{A3}$$

$$\chi_{st}^{(4)pq}(\boldsymbol{k},\tau) \equiv \frac{1}{N}\sum_{\boldsymbol{k}_1\boldsymbol{k}_2}\langle T_\tau c_{p\downarrow}^\dagger(\boldsymbol{k}_1,\tau)c_{q\downarrow}(\boldsymbol{k}_1+\boldsymbol{k},\tau) \times c_{s\downarrow}^\dagger(\boldsymbol{k}_2+\boldsymbol{k},0)c_{t\downarrow}(\boldsymbol{k}_2,0)\rangle, \tag{A4}$$

$$\chi_{st}^{(5)pq}(\boldsymbol{k},\tau) \equiv \frac{1}{N}\sum_{\boldsymbol{k}_1\boldsymbol{k}_2}\langle T_\tau c_{p\uparrow}^\dagger(\boldsymbol{k}_1,\tau)c_{q\downarrow}(\boldsymbol{k}_1+\boldsymbol{k},\tau) \times c_{s\downarrow}^\dagger(\boldsymbol{k}_2+\boldsymbol{k},0)c_{t\uparrow}(\boldsymbol{k}_2,0)\rangle, \tag{A5}$$

$$\chi_{st}^{(6)pq}(\boldsymbol{k},\tau) \equiv \frac{1}{N}\sum_{\boldsymbol{k}_1\boldsymbol{k}_2}\langle T_\tau c_{p\downarrow}^\dagger(\boldsymbol{k}_1,\tau)c_{q\uparrow}(\boldsymbol{k}_1+\boldsymbol{k},\tau) \times c_{s\uparrow}^\dagger(\boldsymbol{k}_2+\boldsymbol{k},0)c_{t\downarrow}(\boldsymbol{k}_2,0)\rangle. \tag{A6}$$

For $U = 0$, we have the bare susceptibility tensors $\chi^{(2)(0)} = \chi^{(3)(0)} = 0$ and

$$\chi_{st}^{(1)(0)pq}(\boldsymbol{k}',i\omega_n) = \frac{1}{N}\sum_{\boldsymbol{k}'\alpha\beta}\xi_{t\uparrow}^{\alpha}(\boldsymbol{k}')\xi_{p\uparrow}^{\alpha*}(\boldsymbol{k}')\xi_{q\uparrow}^{\beta}(\boldsymbol{k}'+\boldsymbol{k}) \times \xi_{s\uparrow}^{\beta*}(\boldsymbol{k}'+\boldsymbol{k})\frac{n_F\left(\varepsilon_{\boldsymbol{k}'+\boldsymbol{k}}^{\beta\uparrow}\right) - n_F\left(\varepsilon_{\boldsymbol{k}'}^{\alpha\uparrow}\right)}{i\omega_n + \varepsilon_{\boldsymbol{k}'}^{\alpha\uparrow} - \varepsilon_{\boldsymbol{k}'+\boldsymbol{k}}^{\beta\uparrow}}, \tag{A7}$$

$$\chi_{st}^{(4)(0)pq}(\boldsymbol{k},i\omega_n)=\frac{1}{N}\sum_{\boldsymbol{k}'\alpha\beta}\xi_{t\downarrow}^{\alpha}(\boldsymbol{k}')\xi_{p\downarrow}^{\alpha*}(\boldsymbol{k}')\xi_{q\downarrow}^{\beta}(\boldsymbol{k}'+\boldsymbol{k})\times\xi_{s\downarrow}^{\beta*}(\boldsymbol{k}'+\boldsymbol{k})\frac{n_F\left(\varepsilon_{\boldsymbol{k}'+\boldsymbol{k}}^{\beta\downarrow}\right)-n_F\left(\varepsilon_{\boldsymbol{k}'}^{\alpha\downarrow}\right)}{i\omega_n+\varepsilon_{\boldsymbol{k}'}^{\alpha\downarrow}-\varepsilon_{\boldsymbol{k}'+\boldsymbol{k}}^{\beta\downarrow}},\quad\text{(A8)}$$

$$\chi_{st}^{(5)(0)pq}(\boldsymbol{k},i\omega_n)=\frac{1}{N}\sum_{\boldsymbol{k}'\alpha\beta}\xi_{t\uparrow}^{\alpha}(\boldsymbol{k}')\xi_{p\uparrow}^{\alpha*}(\boldsymbol{k}')\xi_{q\downarrow}^{\beta}(\boldsymbol{k}'+\boldsymbol{k})\times\xi_{s\downarrow}^{\beta*}(\boldsymbol{k}'+\boldsymbol{k})\frac{n_F\left(\varepsilon_{\boldsymbol{k}'+\boldsymbol{k}}^{\beta\downarrow}\right)-n_F\left(\varepsilon_{\boldsymbol{k}'}^{\alpha\uparrow}\right)}{i\omega_n+\varepsilon_{\boldsymbol{k}'}^{\alpha\uparrow}-\varepsilon_{\boldsymbol{k}'+\boldsymbol{k}}^{\beta\downarrow}},\quad\text{(A9)}$$

$$\chi_{st}^{(6)(0)pq}(\boldsymbol{k},i\omega_n)=\frac{1}{N}\sum_{\boldsymbol{k}'\alpha\beta}\xi_{t\downarrow}^{\alpha}(\boldsymbol{k}')\xi_{p\downarrow}^{\alpha*}(\boldsymbol{k}')\xi_{q\uparrow}^{\beta}(\boldsymbol{k}'+\boldsymbol{k})\times\xi_{s\uparrow}^{\beta*}(\boldsymbol{k}'+\boldsymbol{k})\frac{n_F\left(\varepsilon_{\boldsymbol{k}'+\boldsymbol{k}}^{\beta\uparrow}\right)-n_F\left(\varepsilon_{\boldsymbol{k}'}^{\alpha\downarrow}\right)}{i\omega_n+\varepsilon_{\boldsymbol{k}'}^{\alpha\downarrow}-\varepsilon_{\boldsymbol{k}'+\boldsymbol{k}}^{\beta\uparrow}}.\quad\text{(A10)}$$

In the RPA, we have

$$\begin{pmatrix}\chi^{(1)}\\ \chi^{(3)}\end{pmatrix}=\begin{pmatrix}I & \chi^{(1)(0)}(U)\\ \chi^{(4)(0)}(U) & I\end{pmatrix}^{-1}\begin{pmatrix}\chi^{(1)(0)}\\ 0\end{pmatrix},\quad\text{(A11)}$$

$$\begin{pmatrix}\chi^{(2)}\\ \chi^{(4)}\end{pmatrix}=\begin{pmatrix}I & \chi^{(1)(0)}(U)\\ \chi^{(4)(0)}(U) & I\end{pmatrix}^{-1}\begin{pmatrix}0\\ \chi^{(4)(0)}\end{pmatrix},\quad\text{(A12)}$$

$$\chi^{(5)}=[I-\chi^{(5)(0)}(U)]^{-1}\chi^{(5)(0)},\quad\text{(A13)}$$

$$\chi^{(6)}=[I-\chi^{(6)(0)}(U)]^{-1}\chi^{(6)(0)},\quad\text{(A14)}$$

where (U) is the same as that in Eq. (9).

With the above expressions of $\chi^{(1\sim6)}$, we consider the scattering of a Cooper pair from the state $(\boldsymbol{k}',-\boldsymbol{k}')$ in the βth ($\beta=1,\cdots,4$) band to the state $(\boldsymbol{k},-\boldsymbol{k})$ in the αth ($\alpha=1,\cdots,4$) band. This scattering process leads to the following effective interaction vertices:

$$V_{\uparrow\downarrow}^{\alpha\beta}(\boldsymbol{k},\boldsymbol{k}')=\sum_{pqst}\Gamma_{st\downarrow}^{pq\uparrow}(\boldsymbol{k},\boldsymbol{k}')\xi_{p\uparrow}^{\alpha*}(\boldsymbol{k})\xi_{q\downarrow}^{\alpha*}(-\boldsymbol{k})\xi_{s\downarrow}^{\beta}(-\boldsymbol{k}')\xi_{t\uparrow}^{\beta}(\boldsymbol{k}'),\quad\text{(A15)}$$

$$V_{\uparrow\uparrow}^{\alpha\beta}(\boldsymbol{k},\boldsymbol{k}')=\sum_{pqst}\Gamma_{st\uparrow}^{pq\uparrow}(\boldsymbol{k},\boldsymbol{k}')\xi_{p\uparrow}^{\alpha*}(\boldsymbol{k})\xi_{q\uparrow}^{\alpha*}(-\boldsymbol{k})\xi_{s\uparrow}^{\beta}(-\boldsymbol{k}')\xi_{t\uparrow}^{\beta}(\boldsymbol{k}'),\quad\text{(A16)}$$

where

$$\Gamma_{st\downarrow}^{pq\uparrow}(\boldsymbol{k},\boldsymbol{k}')=(U)_{qs}^{pt}-[(U)\chi^{(3)}(U)]_{qs}^{pt}(\boldsymbol{k}-\boldsymbol{k}')+[(U)\chi^{(6)}(U)]_{qt}^{ps}(\boldsymbol{k}+\boldsymbol{k}'),\quad\text{(A17)}$$

$$\Gamma_{st\uparrow}^{pq\uparrow}(\boldsymbol{k},\boldsymbol{k}')=-\tfrac{1}{2}[(U)\chi^{(4)}(U)]_{qs}^{pt}(\boldsymbol{k}-\boldsymbol{k}')+\tfrac{1}{2}[(U)\chi^{(4)}(U)]_{qt}^{ps}(\boldsymbol{k}+\boldsymbol{k}').\quad\text{(A18)}$$

The inversion symmetry, together with the $U(1)$ spin-rotation symmetry of the system, enables us to symmetrize the effective interaction vertices into the following channels:

$$V_{(e,0)}^{\alpha\beta}(\boldsymbol{k},\boldsymbol{k}')=\tfrac{1}{2}\left[V_{\uparrow\downarrow}^{\alpha\beta}(\boldsymbol{k},\boldsymbol{k}')+V_{\uparrow\downarrow}^{\alpha\beta}(\boldsymbol{k},-\boldsymbol{k}')\right],\quad\text{(A19)}$$

$$V_{(o,0)}^{\alpha\beta}(\boldsymbol{k},\boldsymbol{k}')=\tfrac{1}{2}\left[V_{\uparrow\downarrow}^{\alpha\beta}(\boldsymbol{k},\boldsymbol{k}')-V_{\uparrow\downarrow}^{\alpha\beta}(\boldsymbol{k},-\boldsymbol{k}')\right],\quad\text{(A20)}$$

$$V_{(o,\pm1)}^{\alpha\beta}(\boldsymbol{k},\boldsymbol{k}')=V_{\uparrow\uparrow(\downarrow\downarrow)}^{\alpha\beta}(\boldsymbol{k},\boldsymbol{k}'),\quad\text{(A21)}$$

where the index e is for the even parity pairing, and o is for the odd one. From these symmetrized effective interaction vertices, we obtain the following linearized gap equation near the superconducting critical temperature T_c:

$$-\frac{1}{(2\pi)^2}\sum_{\beta}\oint_{\mathrm{FS}}dk_{\parallel}'\frac{V_{(P,S_z)}^{\alpha\beta}(\boldsymbol{k},\boldsymbol{k}')}{v_F^{\beta}(\boldsymbol{k}')}\Delta_{\beta}(\boldsymbol{k}')=\lambda\Delta_{\alpha}(\boldsymbol{k}),\quad\text{(A22)}$$

which replaces Eq. (13) to determine the T_c and the leading pairing symmetry of the system in the presence of the Kane-Mele SOC.

[1] A. P. Mackenzie and Y. Maeno, Rev. Mod. Phys. **75**, 657 (2003).
[2] N. Read and D. Green, Phys. Rev. B **61**, 10267 (2000).
[3] A. Y. Kitaev, Phys. Usp. **44**, 131 (2001).
[4] E. Stoner, Philos. Mag. **15**, 1018 (1933).
[5] Y. Nagaoka, Phys. Rev. **147**, 392 (1966).
[6] A. Mielke, J. Phys. A: Math. Gen. **24**, L73 (1991).
[7] A. Mielke, J. Phys. A: Math. Gen. **24**, 3311 (1991).
[8] H. Tasaki, Phys. Rev. Lett. **69**, 1608 (1992).
[9] A. Tanaka and H. Tasaki, Phys. Rev. Lett. **98**, 116402 (2007).
[10] L. Liu, H. Yao, E. Berg, S. R. White, and S. A. Kivelson, Phys. Rev. Lett. **108**, 126406 (2012).
[11] H. Katsura and A. Tanaka, Phys. Rev. A **87**, 013617 (2013).
[12] Y. Li, E. H. Lieb, and C. Wu, Phys. Rev. Lett. **112**, 217201 (2014).
[13] S.-S. Zhang, J. Ye, and W.-M. Liu, arXiv:1403.7031.
[14] H. Yao and F. Yang, Phys. Rev. B **92**, 035132 (2015).
[15] B. Lalmi, H. Oughaddou, H. Enriquez, A. Karae, S. Vizzini, B. Ealet, and B. Aufray, Appl. Phys. Lett. **97**, 223109 (2010).
[16] P. Vogt, P. DePadova, C. Quaresima, J. Avila, E. Frantzeskakis, M. C. Asensio, A. Resta, B. Ealet, and G. LeLay, Phys. Rev. Lett. **108**, 155501 (2012).
[17] A. Fleurence, R. Friedlein, T. Ozaki, H. Kawai, Y. Wang, and Y. Yamada-Takamura, Phys. Rev. Lett. **108**, 245501 (2012).
[18] L. Chen, C.-C. Liu, B. Feng, X. He, P. Cheng, Z. Ding, S. Meng, Y. Yao, and K. Wu, Phys. Rev. Lett. **109**, 056804 (2012).
[19] L. Meng, Y. Wang, L. Zhang, S. Du, R. Wu, L. Li, Y. Zhang, G. Li, H. Zhou, W. A. Hofer, and H.-J. Gao, Nano Lett. **13**, 685 (2013).

[20] L. Chen, B. Feng, and K. Wu, Appl. Phys. Lett. **102**, 081602 (2013).
[21] T. P. Kaloni, M. Tahir, and U. Schwingenschlögl, Sci. Rep. **3**, 3192 (2013).
[22] T. P. Kaloni, S. Gangopadhyay, N. Singh, B. Jones, and U. Schwingenschlögl, Phys. Rev. B **88**, 235418 (2013).
[23] W. Wan, Y. Ge, F. Yang, and Y. Yao, Europhys. Lett. **104**, 36001 (2013).
[24] A. P. Durajski, D. Szczęśniak, and R. Szczęśniak, Solid State Commun. **200**, 17 (2014).
[25] G. Baskaran, arXiv:1309.2242.
[26] B. Feng, Z. Ding, S. Meng, Y. Yao, X. He, P. Cheng, L. Chen, and K. Wu, Nano Lett. **12**, 3507 (2012).
[27] F. Liu, C.-C. Liu, K. Wu, F. Yang, and Y. Yao, Phys. Rev. Lett. **111**, 066804 (2013).
[28] T. Li, Europhys. Lett. **97**, 37001 (2012).
[29] M. L. Kiesel, C. Platt, W. Hanke, D. A. Abanin, and R. Thomale, Phys. Rev. B **86**, 020507(R) (2012).
[30] W.-S. Wang, Y.-Y. Xiang, Q.-H. Wang, F. Wang, F. Yang, and D.-H. Lee, Phys. Rev. B **85**, 035414 (2012).
[31] R. Nandkishore, G.-W. Chern, and A. V. Chubukov, Phys. Rev. Lett. **108**, 227204 (2012).
[32] R. Nandkishore, L. S. Levitov, and A. V. Chubukov, Nat. Phys. **8**, 158 (2012).
[33] L.-D. Zhang, F. Yang, and Y. Yao, Sci. Rep. **5**, 8203 (2015).
[34] C. L. Kane and E. J. Mele, Phys. Rev. Lett. **95**, 226801 (2005).
[35] C. L. Kane and E. J. Mele, Phys. Rev. Lett. **95**, 146802 (2005).
[36] C.-C. Liu, H. Jiang, and Y. Yao, Phys. Rev. B **84**, 195430 (2011).
[37] T. Takimoto, T. Hotta, and K. Ueda, Phys. Rev. B **69**, 104504 (2004).
[38] K. Kubo, Phys. Rev. B **75**, 224509 (2007).
[39] K. Kuroki, S. Onari, R. Arita, H. Usui, Y. Tanaka, H. Kontani, and H. Aoki, Phys. Rev. Lett. **101**, 087004 (2008).
[40] S. Graser, T. A. Maier, P. J. Hirschfeld, and D. J. Scalapino, New J. Phys. **11**, 025016 (2009).
[41] T. A. Maier, S. Graser, P. J. Hirschfeld, and D. J. Scalapino, Phys. Rev. B **83**, 100515(R) (2011).
[42] L. C. Hebel and C. P. Slichter, Phys. Rev. **113**, 1504 (1959).
[43] W. D. Knight, G. M. Androes, and R. H. Hammond, Phys. Rev. **104**, 852 (1956).
[44] D. J. Van Harlingen, Rev. Mod. Phys. **67**, 515 (1995).
[45] A. P. Schnyder, S. Ryu, A. Furusaki, and A. W. W. Ludwig, Phys. Rev. B **78**, 195125 (2008).
[46] G. E. Volovik, *The Universe in a Helium Droplet* (Oxford Science Publications, New York, 2003).
[47] X.-L. Qi, T. L. Hughes, S. Raghu, and S.-C. Zhang, Phys. Rev. Lett. **102**, 187001 (2009).